# Shadowgraph investigation of plasma shock wave evolution from Al target under 355-nm laser ablation*

Liu Tian-Hang(刘天航), Hao Zuo-Qiang(郝作强), Gao Xun(高 勋)†,
Liu Ze-Hao(刘泽昊), and Lin Jing-Quan(林景全)‡

*Changchun University of Science and Technology, Changchun* 130022, *China*

(Received 29 November 2013; revised manuscript received 20 May 2014; published online 20 June 2014)

The propagation of a plasma shock wave generated from an Al target surface ablated by a nanosecond Nd:YAG laser operating at 355 nm in air is investigated at the different focusing positions of the laser beam by using a time-resolved shadowgraph imaging technique. The results show that in the case of a target surface set at the off-focus position, the condition of the focal point behind or in front of the target surface greatly influences the evolution of an Al plasma shock wave, and an ionization channel forms in the case of the focal point set in front of the target surface. Moreover, it is found that the shadowgraph with the evolution time around 100 ns shows that a protrusion appears at the front tip of the shock wave if the focal point is at the target surface. In addition, the calculated results of the expanding velocity of the shock wave front, the mass density, and pressure just behind the shock wave front are presented based on the shadowgraphs.

**Keywords:** laser-induced plasma, shock wave, air ionization, off-focus

**PACS:** 52.35.Tc, 52.38.–r, 52.38.Dx, 52.38.Hb **DOI:** 10.1088/1674-1056/23/8/085203

## 1. Introduction

In recent years, due to the fact that the plasma shock wave has been widely used in laser deposition coating, laser shock peening, laser propulsion, and other fields, researchers have paid more and more attention to the dynamic characteristics of plasma shock waves. When a high power laser pulse irradiates a metal surface, the initial part of the laser pulse vaporizes and ionizes the surface of the metal, forming a rapidly expanding hot and dense plasma. This plasma moves into the surrounding atmosphere quite fast and compresses the encountered gas. Most noticeably, the expanding plasma acts as a piston on the surrounding air, driving a shock wave. The propagation of the shock wave reveals some properties such as released energy and refractive index, which can help researchers to understand the interaction between the laser pulse and target materials.

Considerable work has been performed previously on the plasma shock wave and many diagnostic methods have been developed, such as high speed photography,[1] shadowgraphy,[2] interferometry,[3,4] digital holographic interferometry,[5] emission spectroscopy,[6] and acoustical monitoring.[7] Using these diagnostic methods, it is found that laser parameter, target material, ambient gas, and focal point position can strongly affect the plasma shock wave expansion. Amer *et al.*[5] studied the position of the shock wave front induced by 1064-nm laser pulses from a polycrystalline boron nitride target for different focusing conditions. They observed that the induced shock wave without air breakdown had a larger radius than with air breakdown. Zhang *et al.*[8] investigated the collision between the two shock waves induced by laser confined ablation using a time-resolved shadowgraph. It was found that the shock waves did not interact with each other but interacted with the plasma induced by the ablation in the collision. Gravel and Boudreau[9] studied the influences of laser-induced gas breakdown on the extent of laser-sample coupling and the ablation rate with a focal point being above or below the brass shim stock sample surface irradiated by a laser at 1064 nm in argon, air, and helium at atmospheric pressure. They pointed out that the reduced laser-sample coupling was caused by both laser-induced gas breakdown and laser-supported detonation via plasma shielding. Hu *et al.*[10] investigated the early-stage Cu plasma evolution generated by 800-nm femtosecond laser pulses through shadowgraph measurements and simulations. They found that the effect of the focal point position was significant and important for the air breakdown and plasma expansion. Zeng *et al.*[11] studied the propagation of a laser-induced shock wave generated during 266-nm laser pulses ablation in cavities made of fused silica. The development of a cavity during laser ablation led to an increased temperature of the target, stronger laser plasma absorption, and a reduced mass ablation rate. Preuss *et al.*[12] studied the laser ablation of nickel, copper, molybdenum, indium, tungsten, and gold by short ultraviolet laser pulses (0.5 ps, 248 nm). They found that metal ablation in air was

*Project supported by the National Key Basic Research Program, China (Grant No. 2013CB922404), the National Natural Science Foundation of China (Grant Nos. 61178022, 11074027, 11274053, and 11211120156), the Funds from Science and Technology Department of Jilin Province, China (Grant Nos. 20111812 and 20130522149JH), and the Research Fund for the Doctoral Program of Higher Education of China (Grant Nos. 20122216120009, 20122216110007, and 20112216120006).

†Corresponding author. E-mail: lasercust@163.com

‡Corresponding author. E-mail: linjingquan@cust.edu.cn

© 2014 Chinese Physical Society and IOP Publishing Ltd 

significantly less efficient than in a vacuum due to more redeposition of ablated material in air. Boueri *et al.*[13] reported the early stage expansion and interaction with ambient air of the plasma induced by 1064-nm and 266-nm laser pulses on a typical organic sample (nylon). They found that plasma had high transparency for ultra-violet (UV) radiation, while the laser energy reaching the target surface was shielded by the high energy absorption for infra-red (IR) radiation. In an earlier report, we also presented the evolution of a plasma plume from an Al target ablated with a nanosecond 1064-nm and 355-nm lasers respectively at oblique incidence in air with different focusing conditions.[14] It was found that the evolution of the plasma plume was strongly influenced by the laser wavelength in the case of oblique incidence. Up to now, most of the studies have been carried out on the plasma shock wave expansion induced by IR nanosecond laser pulses or femtosecond laser pulses which ablate a fixed-position target under different conditions. Although some researches involve the influences of different positions of the focal point relative to the target surface on plasma shock wave expansion as mentioned above, most of them are performed by using an infra-red (IR) nanosecond laser or a femtosecond laser. The influences of different positions of the focal point relative to the target surface on the plasma expansion dynamics using high power density UV laser pulses has not yet been systematically studied.

In this paper, we present the expansion dynamics of the plasma shock wave induced by high power density UV laser pulses in air using a time-resolved shadowgraph imaging technique. The relative position between the focal point and target surface is varied to investigate the effects of focal point position and the air ionized channel on plasma shock wave expansion.

## 2. Experimental setup

Figure 1 shows a diagram of the experimental setup. A Q-switched Nd:YAG laser (Continuum, Powerlite Precision II) operating at a wavelength of 355 nm with a 5-ns pulse duration is used as the pump beam, which is perpendicularly focused on an Al target with a lens whose focal length is 100 mm ($f = 100$ mm). The pulse energy is attenuated by a combination of a half-wave plate and a polarizer. The laser energy is measured using an energy meter (Coherent, FieldMax II), and the Al target is fixed on a three-dimensional translation stage (SIGMA, SGSP20). The energy of the pump beam is 100 mJ. The aluminum target is polished and cleaned with ethanol before each experiment. Another Nd:YAG laser (Innolas Splitlight Compact 400) operating at a wavelength of 532 nm with an 8-ns pulse duration is delayed to illuminate the expanding plasma from the direction parallel to the target surface, and used as the probe beam for shadowgraphs. This probe beam is expanded by lenses 2 and 3 and directed to a CCD camera (Princeton Instruments Pixis 1024B Detector), which records the time-resolved shadowgraphs of plasma expansion. In this setup, lens 4 is used to image the plasma plume onto the CCD camera. An interference filter with a central wavelength of 532 nm and several neutral density filters are located in front of the CCD camera to block plume radiation and the scattered ablation laser and to protect the CCD camera.

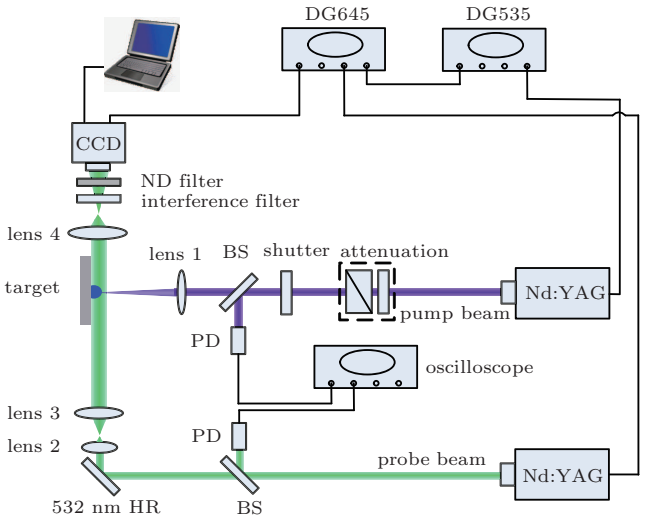



**Fig. 1.** (color online) Schematic diagram of the experimental setup of shadowgraph imaging.

The time delay among pump pulse, probe pulse and CCD camera is controlled by two delay generators (Stanford Research, DG 535 and DG 645). The actual time delay between the pump pulse and the probe pulse is measured by two photodiodes located in each optical path through two beam splitters, and recorded by using an oscilloscope (Tektronix TDS7254B).

## 3. Results and discussion

In order to investigate the effect of the focal point position relative to the target surface on plasma plume expansion, experiments with the focal point set behind, on, and in front of the target surface are carried out. We define $L$ as the distance between lens 1 and the target surface, $f$ the focal length of lens 1, and $d$ the off-focus distance. We prescribe that the direction for the laser focus to be behind the target surface is negative, and in front of the target surface is positive. Figure 2 shows the shadowgraph images of laser-induced plasma from Al in air, which are obtained at different time delays between the pump and probe beams, correspondingly the focal point is at different positions, as shown in the illustrations on the right side of Fig. 2. The rectangular part on the left in each shadowgraph image represents a side view of the Al target, and an arrow on the right is used to indicate the input laser beam. Some weak fringes which appear near the target surface are due to the edge diffraction of the probe beam.

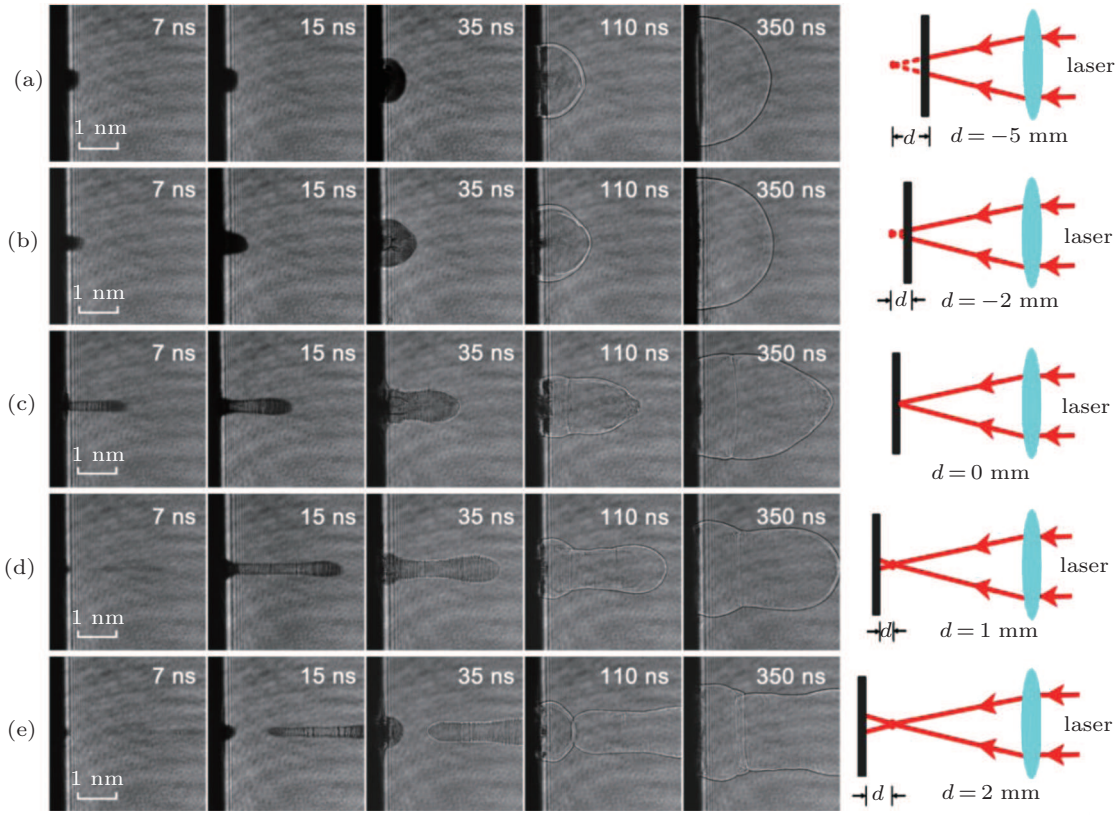



**Fig. 2.** (color online) Shadowgraphs at different times and focal point positions during the evolution of the plasma plume. (a) $d = -5$ mm ($L < f$). (b) $d = -2$ mm ($L < f$). (c) $d = 0$ ($L = f$). (d) $d = 1$ mm ($L > f$). (e) $d = 2$ mm ($L > f$).

Figures 2(a) and 2(b) show the corresponding shadowgraphs of the Al plasma shock wave for the case of $L < f$ ($d = -5$ mm and $-2$ mm respectively). The laser power density on the target surface is $1.05\times10^{10}$ W/cm$^2$ for the case of Fig. 2(a), and it is $3.92\times10^{10}$ W/cm$^2$ for the case of Fig. 2(b). We notice in Figs. 2(a) and 2(b) that the shadowgraphs recorded at the earlier evolution time (for instance, time delay $< 35$ ns) each show a much darker plume region with less details exposed than those taken at the longer time delay, which reflects the higher plasma density at the early stage of its expansion.[15] As the delay time increases, the plasma plume expands in the shape of a hemisphere and shows an obvious feature of a shock wave. Material ejection near the target surface is noticeable as the time delay increases (e.g. 110 ns). Furthermore, it is seen that there are more ejected materials in the case of $d = -2$ mm than that of $d = -5$ mm. The more target ejected materials should be attributed to the higher laser power density imposed on the Al surface for the former case. With a much higher laser power density, the generated shock wave is much stronger and thus has a higher recoil strength to the target, resulting in more ejected materials.

Figures 2(d) and 2(e) show the plasma shock wave evolutions for the case of $L > f$ ($d = 1$ mm and 2 mm respectively). The laser power density at the position of the geometric focal point of lens 1 in air is $1.94\times10^{11}$ W/cm$^2$, and the values on the target surface are $1.65\times10^{10}$ W/cm$^2$ and $7.85\times10^{9}$ W/cm$^2$ for the cases of Figs. 2(d) and 2(e), respectively, where the laser transmission through the breakdown air is considered in the laser power density calculation at the target surface. As shown in the shadowgraph, two sections of plasma plumes appear in Figs. 2(d) and 2(e) at several nanoseconds after laser ablation on the Al target. Particularly, it is clearly shown in Fig. 2(e) that two plasma plumes expand individually at the early stage, forming two shock waves, then these two shock waves meet together at the larger time delay with a clear boundary at the interface, which seems to prevent them from mixing (the case of 110-ns time delay).[16] The hemispherical region near the target surface in Fig. 2(d) or 2(e) is the Al plasma plume generated by the pump laser. Meanwhile, it is observed that starting at about 1 mm (Fig. 2(d) or 2 mm (Fig. 2(e)) away from the front of the target surface, at the corresponding position of the focal point, there forms a column-shape plasma plume, and the length of each column is far beyond the Rayleigh range of the laser beam (0.78 mm in our case). With time increasing beyond the laser pulse duration, the column-shape plasma plume begins to expand in both longitudinal and lateral directions. In our case, the air in the path of the laser beam near the focal point can be ionized under the action of the high intensity 355-nm laser pulse via 4 and 5 photon process (the ionization potentials of $O_2$ and $N_2$ are 12.08 eV and 15.58 eV respectively, and photon energy of 355-nm radiation is 3.5 eV), and the photoionization of

air molecules by 355-nm radiation becomes significant under high laser fluence.[13] Therefore, this column-shape plasma region acts, in fact, as a plasma channel induced by a high-fluence nanosecond UV laser.[13]

By comparison, we notice that the Al plasma plumes shown in Figs. 2(d) and 2(e) are smaller than those in Figs. 2(a) and 2(b). This is attributed to the plasma channel formation in the path of laser propagation. The air ionization before the laser pulse impinges on the Al target results in less pulse energy reaching the target surface. Therefore, a weak ablation occurs in the cases of Figs. 2(d) and 2(e). This is confirmed by observing the optical images of the laser-ablated Al target surface, as shown in Fig. 3. The ablation regions of the Al target shown in Figs. 3(a) and 3(b) are mostly confined near the focal point (the case of best focusing as indicated in Fig. 3(c)); meanwhile, the ablation region becomes greatly spread out as $L > f$ (Figs. 3(d) and 3(e)). The influence of the focusing position on the ablation degree of the Al target is very obvious by comparing the optical images in Fig. 3(b) with those in Fig. 3(e). The focused laser beams on the surface of the target in those two cases should have the same size due to the equal distance of the target surface to the focal point. However, the ablation areas in the two optical images are significantly different. This position-dependent ablation area is mainly caused by a strong absorption of the laser pulse energy in the case of plasma channel formation (Fig. 2(e)), which results in lower laser intensity on the target surface and correspondingly, a smaller volume of material ejection.

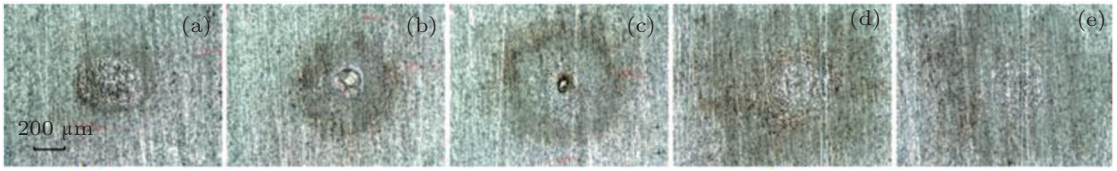



**Fig. 3.** Images of laser ablation spot for the five laser focusing geometries.

In the following experiment, we move the focal point of lens 1 onto the target surface with $L = f$ ($d = 0$). The laser power density on the target surface is $1.94\times10^{11}$ W/cm$^2$. The corresponding shadowgraphs are displayed in Fig. 2(c). The plasma plume in Fig. 2(c) shows a long slender columnar expansion. The columnar plasma plume consists of the Al plasma plume and the plasma channel that is formed before the UV laser pulse impinges on the target. It is surprising to find that the tip of the shock wave front is not smooth, showing a clear protrusion region at the time delay of 110 ns.

In order to investigate the origin of the protrusion at the tip of the shock wave front, the shadowgraphs for shock wave expansion with and without the Al target (only air breakdown occurs) at various time delays are displayed in Figs. 4(a) and 4(b), respectively. It is observed that the tip of the shock wave front with the Al target in Fig. 4(a) always shows a darker protrusion. However, the tip of the shock wave front from air plasma as shown in Fig. 4(b) is quite smooth, without any protrusion observed under the same condition. Therefore, this protrusion shown in Fig. 4(a) is most likely to be caused by the ejected materials from the Al target. When the intense laser pulse ablates on the Al target, the target surface will be overheated and the temperature will rise dramatically. This leads to the formation of an extremely high-temperature and high-pressure plasma in the ablated region, and this high-pressure plasma will be released through the adiabatic expansion. The laser heated area expands outward, inducing a thermoelastic wave which is responsible for the material ejection at longer time delays.[17] Coincidently, the plasma channel due to the UV laser ionization in the air meets the Al plasma, and they are well connected at the very beginning (Fig. 2(c) at 7 ns) and the remaining time delays of the shadowgraphs taken. Moreover, due to the lower pressure inside this channel,[13] the energetic later-ejected materials travel much faster than the shock wave front of air breakdown that travels under one atmospheric pressure, catching up with the shock wave front of air at a certain time delay. These materials accumulate at the shock wave front and break through the shock wave front layer, resulting in the dark protrusion at the front of the shock wave, as shown in the shadowgraphs.[18] As soon as the energetic later-ejected Al materials break through the air shock wave front, they then interact directly with the air, compressing the surrounding air and forming another completed shock wave front at a larger time delay.

The expansion velocity of the shock wave front and the pressure and mass density just behind the shock wave front can be obtained based on the shadowgraphs. The propagation of the laser-induced shock wave can be approximated as resulting from an instantaneous, massless point explosion (blast wave). The expansion distance $R$ between the target surface and the blast wave front depends on the energy converted into the plasma state, $E$.[19] The Sedov–Taylor equation shows the

relation between $R$ and $E$:[20]

$$R = \xi_0 \left(\frac{E}{\rho_1}\right)^{1/(\beta+2)} t^{2/(\beta+2)}, \quad (1)$$

where $\xi_0$ is a constant approximately equal to unity, $\rho_1$ is the mass density of the undisturbed air, $t$ is the time of propagation for the shock wave front after its formation, and $\beta$ is a coefficient related to the dimension of the explosion ($\beta = 1$ for planar propagation, $\beta = 2$ for cylindrical propagation, and $\beta = 3$ for spherical propagation). The conditions which can make this assumption hold true are that the diameter of the spot area of the laser radiation is smaller than $R$ and the pulse duration is shorter than $t$.

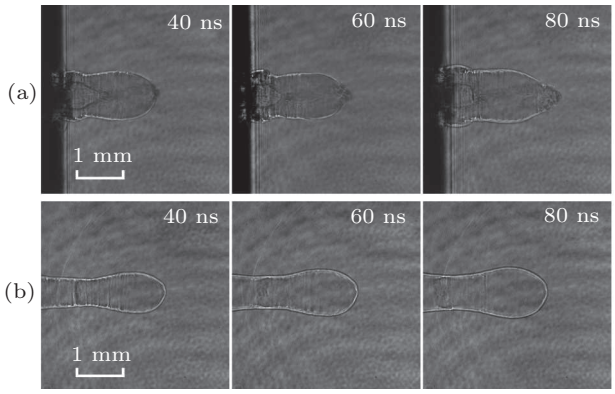



**Fig. 4.** Shadowgraphs at different moments with the target surface at the focal point during the evolution of the plasma plume. (a) With an Al target set at the focal point. (b) Air breakdown only, without an Al target set at the focal point.

For a spherical shock wave, the relation between $R$ and $t$ can be expressed as

$$R = At^{2/5}, \quad (2)$$

where $A$ is a constant that depends on $E$ and $\rho_1$. $A$ can be calculated using the measured values of the distance–time relation of the shock wave front through using Eq. (2). Figure 5(a) shows that the longitudinal expansion distance of the shock wave front generated by the nanosecond laser is proportional to $t^{2/5}$ obtained by using Sedov's point explosion theory for spherical propagation for the cases of $d = -5$ mm and $d = -2$ mm, as is the lateral expansion distance in Fig. 5(b). Triangles and dots represent the measured positions of the shock wave front in shadowgraphs for the cases of $d = -5$ mm and $d = -2$ mm, respectively. The solid lines in Figs. 5(a) and 5(b) represent the fitting curves, which are obtained by using Eq. (2). The results for the cases of $d = -5$ mm and $d = -2$ mm are well fitted to the theoretical equation for our experimental conditions. The slight deviation existing between the measured data and the fitting curve may be attributed to the fact that the laser ablation site is essentially not a real point source.

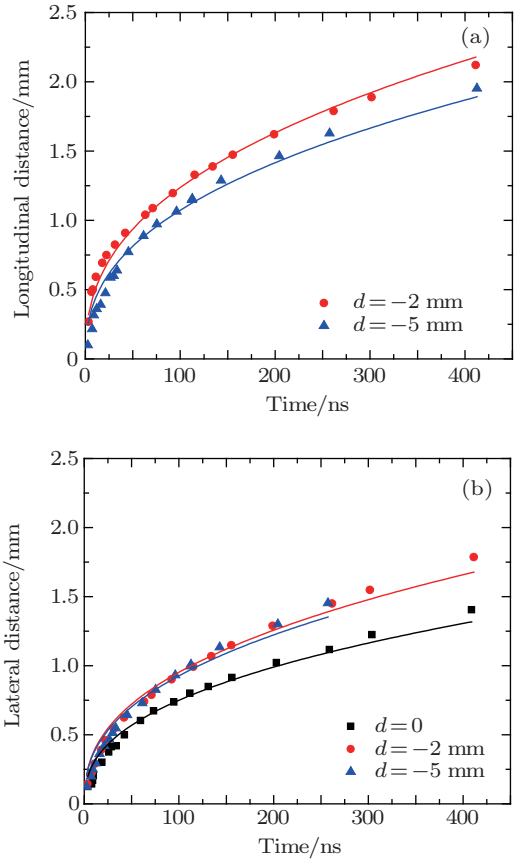



**Fig. 5.** (color online) Longitudinal (a) and lateral (b) distances versus time of shock wave fronts for different target positions. Points represent the measured data and lines represent the expansion distance of the shock wave front calculated according to the Sedov–Taylor equation in Figs. 2(a), 2(b), and 2(c).

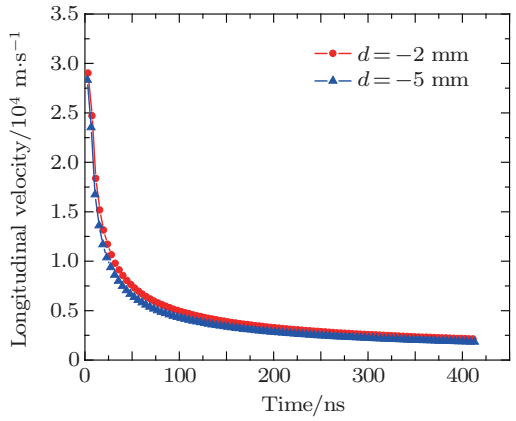



**Fig. 6.** (color online) Calculated longitudinal velocities versus time of the shock wave front for the cases of $d = -5$ mm and $d = -2$ mm.

The longitudinal velocity of the shock wave front for the cases of $d = -5$ mm and $d = -2$ mm can be derived by differentiating Eq. (2), and the plot of longitudinal velocity versus time of the shock wave front is shown in Fig. 6. The expansion velocity of the shock wave front for the case of $d = -2$ mm reaches a value up to $2.90\times10^4$ m/s at the initial stage of expansion, which is a little faster than the velocity of $2.83\times10^4$ m/s for the case of $d = -5$ mm. The velocity decays exponentially in the first 100 ns and then the velocity

reduction becomes slower. The reason for the higher velocity for the case of $d = -2$ mm is attributed to the higher laser power density on the target surface.

Moreover, for an intensive explosion, the pressure ahead of the shock wave may be neglected in comparison with the pressure behind the shock wave. Taking the ambient air around the target as a perfect gas, we can estimate both the mass density and pressure just behind the shock wave front by using the following two equations also developed from Sedov's theory:[21]

$$\rho_2 = \frac{\gamma+1}{\gamma-1}\rho_1\left[1+\frac{2}{\gamma-1}\frac{a_1^2}{v^2}\right]^{-1}, \tag{3}$$

$$p_2 = \frac{2}{\gamma+1}\rho_1 v^2\left[1-\frac{\gamma-1}{2\gamma}\frac{a_1^2}{v^2}\right], \tag{4}$$

where $\rho_2$ and $p_2$ are the mass density and pressure just behind the shock wave front respectively, $\gamma$ is the heat capacity ratio ($\gamma = 1.4$ for air), $\rho_1$ is the mass density of the undisturbed air, $a_1$ is the speed of sound (333 m/s), and $v$ is the speed of the shock wave front, which can be derived from the fitting curve of distance versus time in Fig. 5.

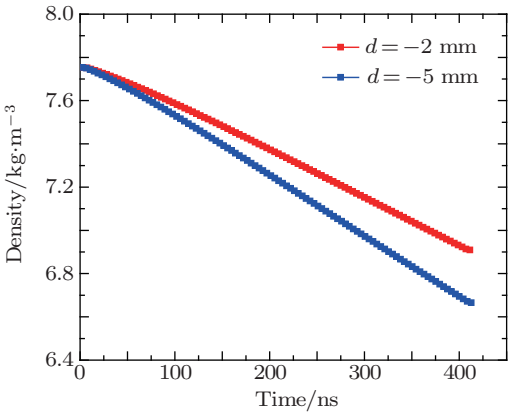



**Fig. 7.** (color online) Calculated air mass densities just behind the shock wave front as a function of time. The calculated results are based on both Eq. (2) and the experimental data from Figs. 2(a) and 2(b).

The calculated mass densities and pressures just behind the shock wave front for different times based on the shadowgraphs of Figs. 2(a) and 2(b) are shown in Figs. 7 and 8, respectively. Figure 7 shows that the mass density just behind the shock wave front decreases slightly as time elapses and the range of density is from 7.75 kg/m$^3$ to 6.6 kg/m$^3$ corresponding to Figs. 2(a) and 2(b). It is also seen that the mass density just behind the shock wave front for the case of $d = -2$ mm is higher than that of $d = -5$ mm, which is because a higher laser power density causes more plasma generation. In Fig. 8, the pressure just behind the shock wave front decreases sharply as time elapses, and the whole pressure for the case of $d = -2$ mm is higher than that of $d = -5$ mm due to higher laser power density. The initial pressure just behind the shock wave front in our experiment for the case of $d = -2$ mm is 777 MPa, while for the case of $d = -5$ mm it is 741 MPa. For the cases of $L = f$ and $L > f$, Sedov's theory is not applicable due to the strong influence of air breakdown on the Al plasma shock wave expansion.

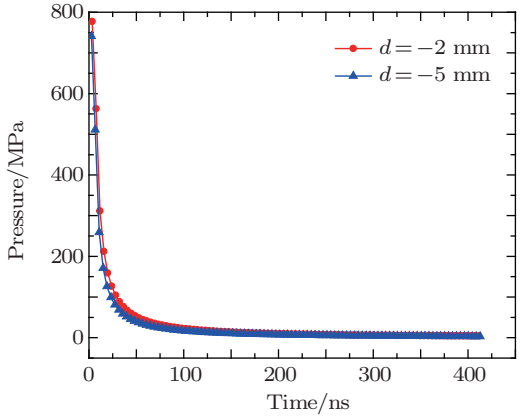



**Fig. 8.** (color online) Calculated air pressures just behind the shock wave front as a function of time. The calculated results are based on both Eq. (2) and the experimental data from Figs. 2(a) and 2(b).

## 4. Conclusions

In this paper, the expansion of plasma shock wave produced by a nanosecond laser operating at 355 nm in air is investigated through using the time-resolved shadowgraph imaging technique. The evolution of plasma shock waves is studied under the conditions of the focal point set behind, on, and in front of the target surface. An ionized channel of air is generated due to the high intensity and high photon energy of 355-nm laser pulses focusing in the air when the focal point is on and in front of the target surface, and a protrusion is observed at the tip of the shock wave front of air in the shadowgraphs when the focal point is on the target surface, resulting from the ejected materials of the Al target, which catch up with the tip of the shock wave front of air. It is also observed that the Al plasma plume shows spherical expansion with the focal point set behind the target surface, while two plasma plumes, that are caused by air breakdown and Al ablation respectively, are generated with the focal point set in front of the target surface. At the initial stage of expansion, the calculated expanding velocity of the shock wave front reaches a value up to $2.90\times10^4$ m/s, and the mass density and pressure just behind the shock wave front are 7.75 kg/m$^3$ and 777 MPa respectively for the case of the focal point set 2 mm behind the target surface.

## References

[1] Maher W E, Hall R B, Johnson R R 1974 *J. Appl. Phys.* **45** 2138
[2] Mao S S, Mao X L, Greif R and Russo R E 2000 *Appl. Phys. Lett.* **77** 2464
[3] Villagrán-Muniz M, Sobral H and Camps E 2001 *IEEE Trans. Plasma Sci.* **29** 613
[4] Schönherr T, Nees F, Arakawa Y, Komurasaki K and Herdrich G 2013 *Phys. Plasmas* **20** 033503

[5] Amer E, Gren P and Sjödahl M 2008 *J. Phys. D: Appl. Phys.* **41** 215502
[6] Ma Q L, Motto-Ros V, Laye F, Yu J, Lei W Q, Bai X S, Zheng L J and Zeng H P 2012 *J. Appl. Phys.* **111** 053301
[7] Stauter C, Gérard P, Fontaine J and Engel T 1997 *Appl. Surf. Sci.* **109/110** 174
[8] Zhang Y, Zheng Z Y, Li Y T, Liu F, Li H M, Lu X and Zhang J 2007 *Acta Phys. Sin.* **56** 5931 (in Chinese)
[9] Gravel J F Y and Boudreau D 2009 *Spectr. Acta: Part B* **64** 56
[10] Hu W, Shin Y C and King G 2011 *Phys. Plasmas* **18** 093302
[11] Zeng X Z, Mao X L, Mao S S, Wen S, Greif R and Russo R E 2006 *Appl. Phys. Lett.* **88** 061502
[12] Preuss S, Demchuk A and Stuke M 1995 *Appl. Phys. A* **61** 33
[13] Boueri M, Baudelet M, Yu J, Mao X L, Mao S S and Russo R E 2009 *Appl. Surf. Sci.* **255** 9566
[14] Liu T H, Gao X, Hao Z Q, Liu Z H and Lin J Q 2013 *J. Phys. D: Appl. Phys.* **46** 485207
[15] Harilal S S, Miloshevsky G V, Diwakar P K, LaHaye N L and Hassanein A 2012 *Phys. Plasmas* **19** 083504
[16] Zhang Y, Li Y T, Zheng Z Y, Liu F, Zhong J Y, Lin X X, Liu F, Lu X and Zhang J 2007 *Chin. Phys.* **16** 3728
[17] Zhang N, Zhu X N, Yang J J, Wang X L and Wang M W 2007 *Phys. Rev. Lett.* **99** 167602
[18] Li Y T, Zhang J, Teng H, Li K, Peng X Y, Jin Z, Lu X, Zheng Z Y and Yu Q Z 2003 *Phys. Rev. E* **67** 056403
[19] Zeng X Z, Mao X L, Greif R and Russo R E 2005 *Appl. Phys. A* **80** 237
[20] Sedov L I 1993 *Similarity and Dimensional Methods in Mechanics*, 10th edn. (Boca Raton: CRC Press) p. 193
[21] Sedov L I 1993 *Similarity and Dimensional Methods in Mechanics*, 10th edn. (Boca Raton: CRC Press) p. 261